*Journal of Sound and Vibration* (1997) **203**(4), 667–695

# AN EQUIVALENT SOURCE METHOD FOR CALCULATION OF THE SOUND RADIATED FROM AIRCRAFT ENGINES

F. HOLSTE†

*Deutsche Forschungsanstalt für Luft- und Raumfahrt e.V., Abteilung Turbulenzforschung, Berlin, Müller-Breslau-Str. 8, D-10623 Berlin, Germany*

(*Received* 27 *November* 1995, *and in final form* 16 *December* 1996)

A theoretical/numerical method is described to predict the radiated sound field of a propfan model by using the pressure fluctuations measured in the exit plane (near field). The prediction scheme is based on the equivalent source method, which is extended to include the effects of the mean flow conditions of an aircraft engine. In a first model, a uniform flow is assumed in the jet exit flow as well as in the external flow. The comparison between the calculated and measured sound fields shows good agreement for the maximum sound pressure levels, but differences were observed in the directivity characteristics, which are mainly caused by the different velocities in the jet and the external flow (wind tunnel flow). To account approximately for the non-uniform flow conditions, the total sound field was divided into two regions with different velocities. Different sets of equivalent sources were employed to describe the sound propagation in the first two flow regions. With this model, very good agreement was achieved between predicted and measured maximum sound levels as well as directivity characteristics. The prediction method can in principle be applied to arbitrary geometries and, therefore, also to other aeroengines, such as compressors, fans and turbines.



## 1. INTRODUCTION

In the next generation of civil aircraft engines on large airplanes, the bypass ratio will be increased to achieve a reduction of the specific fuel consumption as well as exhaust emission. At the same time the noise emission of the jet flow from the core engine will be reduced, so that the fan, which generates the high bypass flow, will become an important noise source on future engines. Therefore, considerations about the aerodynamic noise generation mechanisms of the fan and the expected noise emission should be taken into account in order to develop aircraft engines with low noise levels.

One conceptual design of future high bypass aircraft engine, which has been introduced by MTU (Motoren- und Turbinen Union München) using the technological concept CRISP (Counter-Rotating Integrated Shrouded Propfan), is shown in Figure 1. In this concept the bypass ratio is increased up to 1:20 with a predicted saving in specific fuel consumption of nearly 20% in comparison with today's modern engines that have a bypass ratio of the order of 1:6. The bypass flow is generated by two counter-rotating rotors, which are driven by a core engine. The shroud is supported by struts located downstream of the rotors. The core engine will be the same as in existing engines; only the rotor system driving the bypass flow is to be newly designed. A scaled down model with a 400 mm rotor diameter, which is shown in Figure 2, was constructed by MTU for aerodynamic and

† Now at BMW Rolls-Royce AeroEngines, Eschenweg 11, 15827 Dahlewitz, Germany.

0022–460X/97/240667 + 29 $25.00/0/sv960891 

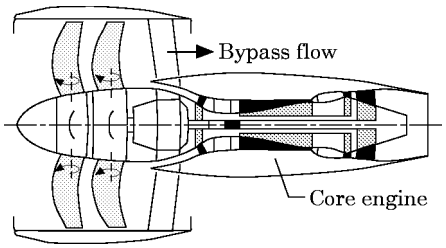


Figure 1. A schematic description of the CRISP aircraft engine.

acoustic testing. In this propfan model, the two counter-rotating rotors are driven by a compressed air turbine instead of a core engine.

Acoustical investigations of the propfan model have been carried out in the open test section of the German-Dutch Wind Tunnel (Deutsch–Niederländischer Windkanal, DNW); see Figure 3. To explore the dominant aerodynamic noise generation mechanism, the pressure fluctuations in the exit plane (near field) are measured by using a suitable microphone traversing system, and are then resolved numerically into acoustical

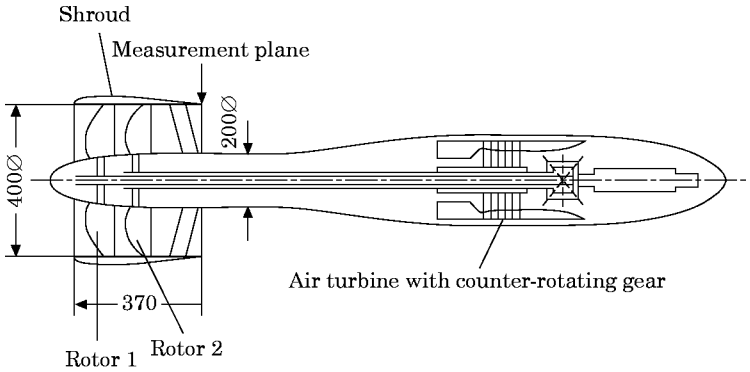


Figure 2. A schematic of the CRISP 0·4 m propfan model.

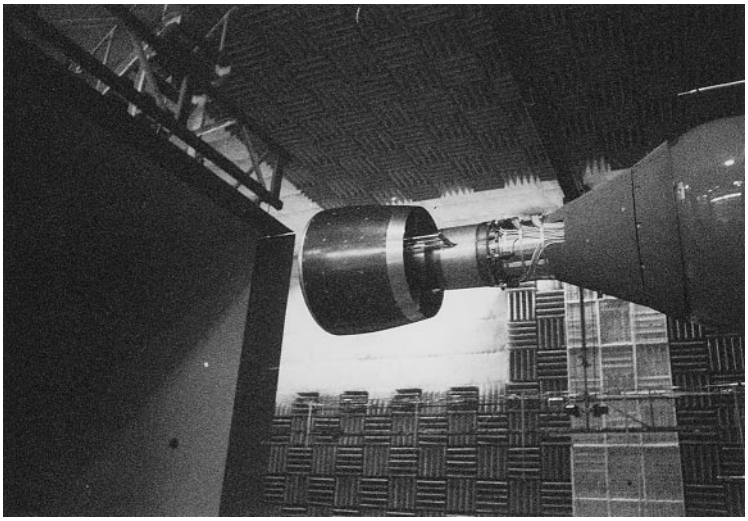

Figure 3. The experimental set-up in the open test section of the German–Dutch Wind Tunnel (DNW).

modes for each tone component. The dominant modes in the mode distributions allow conclusions about their generation mechanism; for more details, see references [1, 2]. Acoustical far field measurements are performed by the DLR in Braunschweig for a determination of the radiated sound field, which are used for a prediction of the noise levels of the future propfan; see reference [3]. Therefore, a calculation of the radiated sound field is not necessary in this case.

However, the aerodynamic performance of models of aircraft engines, or of full size engines, is often tested in small wind tunnels or other test facilities, which do not provide ideal acoustic measurement conditions (acoustic free field conditions) for an experimental determination of the noise emission, because sound reflections at walls and other test installations disturb far field measurements. Also, the measurement microphones cannot be placed far enough from the engine to meet the requirements of acoustical and geometrical far field conditions. Compared to that, the pressure fluctuations in the acoustic near field, i.e., in the exit plane, are largely independent of the acoustical environment and can therefore be used for a prediction of the noise emission from the aircraft engine. In this paper, a theoretical/numerical approach is described to determine the radiated sound field by using the pressure fluctuations measured in the exit plane of the propfan. The influence of the non-uniform flow on the sound radiation is accounted for approximately. The application of this approach to the CRISP 0·4 m propfan model described above showed good agreement between the calculated sound radiation and the results of the far field measurements. The calculation method is based on the equivalent source method.

## 2. EQUIVALENT SOURCE METHOD

The basic idea of the equivalent source technique is to replace the radiating body by a system of simple sources located inside the envelope of the radiator. In recent years, various authors [4–14] have applied the equivalent source method successfully to different radiation problems without flow. These papers differ in the number and type of sources which are used, and also in the calculation method for the determination of the source strength distribution. However, the principle of the equivalent source method is similar in all papers, and will be derived by using Figure 4, where a sound-radiating body with arbitrary shape is shown. $S_k$ denotes the surface of the body. The pressure fluctuations $p'$ are described by

$$p' = \mathrm{Re}\,\{p\,\mathrm{e}^{-\mathrm{i}\omega t}\}, \tag{1}$$

where $p$ is the complex sound pressure, $\omega$ is the circular frequency, $\mathrm{i} = \sqrt{-1}$ and $t$ denotes the time. For simplicity, the real part $\mathrm{Re}\,\{\cdots\}$ is omitted in the following equations. The

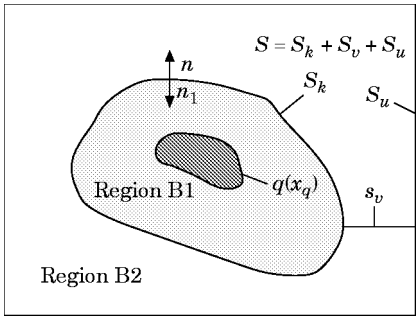


Figure 4. The equivalent source method.

sound radiation from the surface $S_k$ into the region B2 is given by the Kirchhoff–Helmholtz equation [4, 15]:

$$p_2(x_i) = \int_V 0 \, \mathrm{d}V - \oint_S \left( p(x_s) \frac{\partial g(x_i - x_s)}{\partial n} - g(x_i - x_s) \frac{\partial p(x_s)}{\partial n} \right) \mathrm{d}S. \tag{2}$$

$x_i$ is an arbitrary point in region B2, $p(x_s)$ describes the complex pressure on the surface $S$ and $x_s$ represents the co-ordinates of the surface $S$. $\partial/\partial n$ denotes the derivative normal to the surface. In this case no sources exist in the region B2 and therefore the volume integral over $V$ is zero. $g$ is the Green function, which is a solution of the harmonic wave equation

$$k^2 g + \Delta g = \delta(x_i - x_q), \tag{3}$$

with the Dirac function $\delta(\cdots)$ as source term. $k = \omega/a$ is the wavenumber, $a$ denotes the sound speed and $\Delta$ represens the Laplace operator. The surface $S$ surrounds the whole region B2 and consists of $S_k + S_v + S_u$; see Figure 4. In this investigation sound radiation into free space (free field) is considered, and therefore the surface $S_u$ is chosen infinitely far away from the body and the integration over $S_v$ runs in both directions. This means that the integrals over $S_u$ and $S_v$ vanish, and $S$ can be replaced by $S_k$ in equation (2). The remaining surface integral can be transformed to a volume integral over the source region $q(x_q)$, which is inside of the surface $S_k$ (see Figure 4) by using the following consideration. Applying the Kirchhoff–Helmholtz equation to the region B1 leads to

$$\left.\begin{matrix} p_1(x_i) \text{ in B1} \\ 0 \text{ in B2} \end{matrix}\right\} = \int_V q(x_q) g(x_i - x_q) \, \mathrm{d}V - \oint_{S_k} \left( p(x_s) \frac{\partial g(x_i - x_s)}{\partial n_1} - g(x_i - x_s) \frac{\partial p(x_s)}{\partial n_1} \right) \mathrm{d}S. \tag{4}$$

$x_q$ represents the co-ordinates of the source distribution $q(x_q)$ and the sound field in the region B1 is described by $p_1(x_i)$, if $x_i$ is inside of B1. In the region B2, $p_1(x_i) = 0$ and hence the surface integral is equal to the volume integral of equation (4):

$$\int_V q(x_q) g(x_i - x_q) \, \mathrm{d}V = \oint_{S_k} \left( p(x_s) \frac{\partial g(x_i - x_s)}{\partial n_1} - g(x_i - x_s) \frac{\partial p(x_s)}{\partial n_1} \right) \mathrm{d}S \qquad \text{with } x_i \in \text{B2}. \tag{5}$$

The surface integrals are equal in equations (2) and (5), except for the opposite direction of the normal derivatives $\partial/\partial n$ and $\partial/\partial n_1$ ($S = S_k$). Introducing equation (5) into equation (2) gives, for the radiated sound field in region B2,

$$p_2(x_i) = \int_V q(x_q) g(x_i - x_q) \, \mathrm{d}V. \tag{6}$$

Equation (6) shows that the sound radiation of a body with the surface $S_k$ can be described by an equivalent source distribution $q(x_q)$. In practical application of the equivalent source method the integral in equation (6) is replaced by a sum of "simple" sources, called the equivalent sources $q_j$, which are enclosed by the surface $S_k$ and are located at $x_{qj}$:

$$p_2(x_i) \approx \sum_{j=1}^{N_q} q_j g(x_i - x_{qj}). \tag{7}$$

$N_q$ is the number of equivalent source and the source strength $q_j$ can be calculated by using the boundary condition on the surface $S_k$: equation (7) describes the pressure in the whole region B2 and, consequently, also very close to the surface $S_k$, where the pressure fluctuations and their derivative in the normal direction can be assumed to be equal to $p(x_s)$ and its derivative:

$$p_2(x_s) \approx \sum_{j=1}^{N_q} q_j g(x_s - x_{qj}), \qquad \frac{\partial p_2(x_s)}{\partial n} \approx \sum_{j=1}^{N_q} q_j \frac{\partial g(x_s - x_{qj})}{\partial n} \tag{8}$$

Equations (8) show that the strengths of the equivalent sources $q_j$ can be estimated if over the whole surface $S_k$ the pressure fluctuations $p_2(x_s)$ or its normal derivative $\partial p_2(x_s)/\partial n$ is known. $\partial p_2(x_s)/\partial n$ is proportional to the normal component of the particle velocity $v_n$ or the displacement $h_n$ [16, 17]:

$$v_n = (-\mathrm{i}/\rho\omega)\, \partial p_2(x_s)/\partial n, \qquad h_n = (1/\rho\omega^2)\, \partial p_2(x_s)/\partial n. \tag{9}$$

$\rho$ denotes the density of the medium. For a numerical solution, the surface $S_k$ is divided into $N_s$ boundary elements to establish a set of $N_s$ linear equations by using equations (8). Usually, more surface elements are chosen than equivalent sources ($N_s > N_q$) and in this investigation the system of equations is solved by using the least squares fit method, which minimizes the quadratic differences between the given and calculated values on the surface $S_k$:

$$\sum_{\ell=1}^{N_{s1}} \left| p_2(x_{s\ell}) - \sum_{j=1}^{N_q} q_j g(x_{s\ell} - x_{qj}) \right|^2 = \min, \qquad \sum_{l=1}^{N_{s2}} \left| \frac{\partial p_2(x_{s\ell})}{\partial n} - \sum_{j=1}^{N_q} q_j \frac{\partial g(x_{s\ell} - x_{qj})}{\partial n} \right|^2 = \min. \tag{10}$$

$N_{s1}$ and $N_{s2}$ denote the numbers of surface elements on which the pressure $p_2(x_s)$ and the normal derivative $\partial p_2(x_s)/\partial n$ are known respectively.

In summary, it has been shown here that the sound radiation of a body is described by a set of equivalent sources located inside the radiator, if these sources generate the same pressure fluctuations on the surface $S_k$ as the radiator itself. This condition can be satisfied by using different types and numbers of equivalent sources. Also, there exists no unique solution for the positions of the sources inside of the radiator: i.e., different distributions of the sources can be used for the calculation of the sound field radiation.

## 3. RING SOURCES AS EQUIVALENT SOURCES

In this study, ring sources are used as equivalent sources for calculation of the sound radiation, because of the circular geometry of the propfan model; compare with the schematic presentation in Figure 5. The ring sources are located in the interior of the aircraft engine, and their strengths are calculated by using the boundary conditions on the propfan surface and in the exit plane. As described in section 2, only *one* of the acoustical parameters—pressure, particle velocity or displacement—must be known over the whole surface; knowledge of the actual aeroacoustic noise generation mechanisms is not required. In the present case the boundary conditions used are the measured pressure fluctuations (mode distribution) in the exhaust plane and the condition of vanishing acoustic velocity at the rigid walls of the hub and the shroud. Unfortunately, no information is available on the acoustic fluctuations in the inlet plane, and thus, only the sound radiation from the exhaust plane can be predicted.

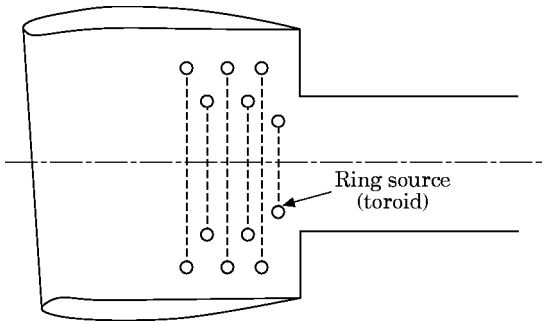


Figure 5. Equivalent ring sources in an aircraft engine.

For each frequency $\omega$, the pressure fluctuations $p'$ in the near and far field are described in cylindrical co-ordinates $x, r, \varphi$ and can be resolved into a distribution of circumferential modes $\tilde{p}_m(x, r)$ at each axial and radial position $x, r$:

$$p'(x, r, \varphi, t) = \sum_{m=-\infty}^{\infty} \tilde{p}_m(x, r)\, \mathrm{e}^{\mathrm{i}m\varphi}\, \mathrm{e}^{-\mathrm{i}\omega t}. \tag{11}$$

By analogy, the ring sources are described by a sum over the circumferential source components $Q_m(x, r)$:

$$Q'(x, r, \varphi, t) = \sum_{m=-\infty}^{\infty} Q_m(x, r)\, \mathrm{e}^{\mathrm{i}m\varphi}\, \mathrm{e}^{-\mathrm{i}\omega t}, \qquad \text{with } Q_m(x, r) = \tilde{q}_m\, \delta(x - x_q)\, \delta(r - r_q). \tag{12}$$

$x_q$ and $r_q$ denote the position of the ring source (see Figure 6) and $\tilde{q}_m$ represents the strength of the source. The acoustic wave equation in cylindrical co-ordinates [18] for the no-flow case is

$$\frac{1}{a^2}\frac{\partial^2 p'}{\partial t^2} - \frac{\partial^2 p'}{\partial x^2} - \frac{1}{r}\frac{\partial}{\partial r}\left(r\frac{\partial p'}{\partial r}\right) - \frac{1}{r^2}\frac{\partial^2 p'}{\partial \varphi^2} = Q'(x, r, \varphi, t). \tag{13}$$

By using the superposition principle the sound radiation is calculated for each circumferential order $m$. Inserting equations (11) and (12) into the acoustic wave equation (13) leads to

$$-k^2\tilde{p}_m - \frac{\partial^2 \tilde{p}_m}{\partial x^2} - \frac{1}{r}\frac{\partial}{\partial r}\left(r\frac{\partial \tilde{p}_m}{\partial r}\right) + \frac{m^2}{r^2}\tilde{p}_m = Q_m. \tag{14}$$

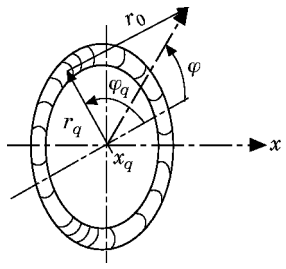


Figure 6. The ring source (torus).

$\tilde{p}_m$ and $Q_m$ are independent of the circumferential angle $\varphi$, and equation (14) is reduced to the two dimensions $x$ and $r$.

The radiated sound field of a ring source without flow was derived by Fuchs and Michalke [19, 20]:

$$\tilde{p}_m = \tilde{q}_m \frac{r_q}{4\pi} \int_0^{2\pi} \frac{e^{ikr_0}}{r_0} e^{im\chi} \, d\chi \qquad \text{with } r_0 = \sqrt{(x - x_q)^2 + r^2 + r_q^2 - 2rr_q \cos(\chi)}. \tag{15}$$

Here, $\chi = \varphi - \varphi_q$ and $r_0$ denote the angular separation and the distance, respectively, between a ring source element and the field point $x, r, \varphi$ considered; see Figure 6. Rearranging terms gives

$$\tilde{p}_m = q'_m \Pi'_m \qquad \text{with } q'_m = \tilde{q}_m r_q / 2\pi, \qquad \Pi'_m = \int_0^{\pi} \frac{e^{ikr_0}}{r_0} \cos(m\chi) \, d\chi. \tag{16}$$

The integral for the radiation function $\Pi'_m$ accounts for three-dimensional radiation characteristic.

For an approximate consideration of the flow conditions around the propfan model, ring sources in uniform flow are used as equivalent sources. The sound radiation of such sources are derived by using the convective flow equation [18]:

$$\frac{1}{a^2}\left(\frac{\partial}{\partial t} + U\frac{\partial}{\partial x}\right)^2 p' - \frac{\partial^2 p'}{\partial x^2} - \frac{1}{r}\frac{\partial}{\partial r}\left(r\frac{\partial p'}{\partial r}\right) - \frac{1}{r^2}\frac{\partial^2 p'}{\partial \varphi^2} = Q''(x, r, \varphi, t). \tag{17}$$

when $a$ is the sound speed, $U$ denotes the speed of the uniform flow and the flow direction is parallel to the $x$ co-ordinate. Similarly to equation (12), the ring sources are described by

$$Q''(x, r, \varphi, t) = \sum_{m=-\infty}^{\infty} q''_m \, \delta(x - x_q) \, \delta(r - r_q) e^{im\varphi} \, e^{-i\omega t}. \tag{18}$$

By introducing the Mach number $M = U/a$, $\beta = \sqrt{1 - M^2}$ and using the co-ordinate transformation (Lorentz transformation) described in references [21, 22]

$$Z = x/\beta, \qquad T = at\beta + M_x/\beta, \tag{19}$$

equation (17) can be rewritten to become

$$\frac{\partial^2 p'}{\partial T^2} - \frac{\partial^2 p'}{\partial Z^2} - \frac{1}{r}\frac{\partial}{\partial r}\left(r\frac{\partial p'}{\partial r}\right) - \frac{1}{r^2}\frac{\partial^2 p'}{\partial \varphi^2} = Q''(Z, r, \varphi, T), \tag{20}$$

and a transformation of the source term (equation (18)) leads to

$$Q''(Z, r, \varphi, T) = \sum_{m=-\infty}^{\infty} q''_m \, \delta(Z\beta - x_q) \, \delta(r - r_q) \, e^{im\varphi} \, e^{-iK(T - MZ)} \qquad \text{with } K = k/\beta. \tag{21}$$

By using the standard relations for the Dirac functions [4] the expression $\delta(Z\beta - x_q)$ can be rewritten to become

$$\delta\{(\beta(Z - Z_q)\} = (1/\beta) \, \delta\{(Z - Z_q)\}, \qquad \text{with } Z_q = x_q/\beta, \tag{22}$$

which leads to

$$Q''(Z, r, \varphi, T) = \sum_{m=-\infty}^{\infty} (q''_m/\beta)\, \delta(Z - Z_q)\, \delta(r - r_q)\, \mathrm{e}^{\mathrm{i}m\varphi}\, \mathrm{e}^{-\mathrm{i}K(T - MZ)}$$

$$= \sum_{m=-\infty}^{\infty} (q''_m/\beta)\, \mathrm{e}^{\mathrm{i}KMZ_q}\, \delta(Z - Z_q)\, \delta(r - r_q)\, \mathrm{e}^{\mathrm{i}m\varphi}\, \mathrm{e}^{-\mathrm{i}KT} \qquad (23).$$

One can expect that

$$p'(Z, r, \varphi, T) = \sum_{m=-\infty}^{\infty} p_m(Z, r)\, \mathrm{e}^{\mathrm{i}m\varphi}\, \mathrm{e}^{-\mathrm{i}KT} \qquad (24)$$

is a solution of equation (20). According to the superposition principle, and introducing equations (23) and (24) into equation (20), one obtains, for each order $m$,

$$-K^2 p_m - \frac{\partial^2 p_m}{\partial Z^2} - \frac{1}{r}\frac{\partial}{\partial r}\left(r\frac{\partial p_m}{\partial r}\right) + \frac{m^2}{r^2} p_m = \frac{q''_m}{\beta}\, \mathrm{e}^{\mathrm{i}KMZ_q}\, \delta(Z - Z_q)\, \delta(r - r_q). \qquad (25)$$

The equation has a form similar to equation (14), with the source term $Q_m$ described in equation (12) for the no-flow case. The sound radiation of equation (12) is given by equation (16). Comparing the variables in equation (25) to those in equation (14) and introducing the result into equation (16) leads to

$$p_m = q''_m \frac{r_q}{2\pi\beta}\, \mathrm{e}^{\mathrm{i}KMZ_q} \int_0^{\pi} \frac{\mathrm{e}^{\mathrm{i}KR_0}}{R_0} \cos(m\chi)\, \mathrm{d}\chi,$$

$$\text{with } R_0 = \sqrt{(Z - Z_q)^2 + r^2 + r_q^2 - 2rr_q \cos(\chi)}, \qquad (26)$$

and one obtains, by using equation (24)

$$p'(Z, r, \varphi, T) = \sum_{m=-\infty}^{\infty} q''_m \frac{r_q}{2\pi\beta}\, \mathrm{e}^{-\mathrm{i}K(T - MZ_q)}\, \mathrm{e}^{\mathrm{i}m\varphi} \int_0^{\pi} \frac{\mathrm{e}^{\mathrm{i}KR_0}}{R_0} \cos(m\chi)\, \mathrm{d}\chi. \qquad (27)$$

A re-transformation gives

$$p'(x, r, \varphi, t) = \sum_{m=-\infty}^{\infty} p_m(x, r)\, \mathrm{e}^{\mathrm{i}m\varphi}\, \mathrm{e}^{-\mathrm{i}\omega t}, \qquad (28)$$

where

$$p_m(x, r) = q_m \Pi_m(x, r) \qquad \text{with } q_m = q''_m \frac{r_q}{2\pi\beta},$$

$$r_0 = \sqrt{\frac{(x - x_q)^2}{1 - M^2} + r^2 + r_q^2 - 2rr_q \cos(\chi)},$$

$$\text{and } \Pi_m(x, r) = \mathrm{e}^{-\mathrm{i}[M/(1 - M^2)]k(x - x_q)} \int_0^{\pi} \frac{\mathrm{e}^{\mathrm{i}(k/\beta)r_0}}{r_0} \cos(m\chi)\, \mathrm{d}\chi. \qquad (29)$$

Equations (28) and (29) describe the sound field of a ring source in a uniform flow in the $x$-direction. These types of sources with the source strength $q_m$ and the radiation function $\Pi_m$ are used for the calculation of the sound radiation as is shown in sections 6 and 7. The integral in equation (29) is solved numerically during the calculations.

## 4. THE EXPERIMENTAL SET-UP

A schematic view of the propfan model is given by Figure 2, and in Figure 3 is shown the propfan installed in the open test section of the German–Dutch Wind Tunnel. The two counter-rotating rotors are $2R = 0{\cdot}4\,m$ in diameter and are driven by a compressed air turbine via a spider gear. Each rotor has ten blades and the shroud is supported by seven struts located downstream of the second rotor. The radius of the exit plane is $R = 0{\cdot}2\,m$ and the hub-to-tip ratio is $\eta = 0{\cdot}5$. Measurements under five different operational conditions of the propfan model, which are summarized in Table 1 are considered in this paper. The relative pressure ratio $\pi_{rel}$ of the propfan is given by

$$\pi_{rel} = [P_{t2}/P_{t1} - 1]/[P_{t2}/P_{t1})_0 - 1], \tag{30}$$

where $P_{t1}$ and $P_{t2}$ denote the total pressures at the inlet and exit of the propfan model, respectively, and $(P_{t1}/P_{t2})_0$ represents the pressure ratio at the design point. Maximum thrust is obtained at $\pi_{rel} = 1$.

### 4.1. NEAR FIELD MEASUREMENTS

For the unsteady pressure measurements, a microphone traversing system was mounted directly on the hub behind the exit plane; see Figure 7. There are two microphone rakes placed on a rotatable cylinder at 180° angular distance. Six small DC motors and a gear drive were used to move the cylinder together with the microphones in the circumferential direction. With this arrangement, the pressure fluctuations were measured at 120 equally spaced angular positions ($\Delta\varphi = 3^\circ$). Each rake carries three 1/4 inch microphones with nose cones at the radial positions $r/R = 0{\cdot}96$, $0{\cdot}785$ and $0{\cdot}61$. The measurements plane was inside of the shroud with 10 mm axial distance to exit plane. The maximum flow Mach number in the exit plane was $M = 0{\cdot}61$ and the maximum wind tunnel flow speed was $M = 0{\cdot}22$.

### 4.2. DATA ACQUISITION AND MODE ANALYSIS

For the acoustic mode analysis, the circumferential and radial distributions of both the magnitude and the phase of each spectral component of interest need to be known. Three two-channel FFT analyzers (HP-3562A) were used to measure the spectra of the six

TABLE 1

*Five different operating conditions of the propfan model, for which comparisons between the calculated and measured radiated sound field are carried out*

| Operating point | 21/02 | 21/07 | 21/10 | 21/09 | 21/04 |
|---|---|---|---|---|---|
| Pressure ratio, $\pi_{rel}$ | 1·0 | 0·8 | 0·8 | 0·4 | 0·4 |
| Blade stagger angle, $\psi$ | $-6^\circ/-6^\circ$ | $-6^\circ/-6^\circ$ | $-6^\circ/-6^\circ$ | $-6^\circ/-6^\circ$ | $-8^\circ/-8^\circ$ |
| Mach number of the wind tunnel flow, $M$ | 0·22 | 0·15 | 0·22 | 0·22 | 0·22 |
| Non-dimensional blade passing frequency, $kR$ | 7·07 | 6·31 | 6·46 | 4·81 | 5·04 |

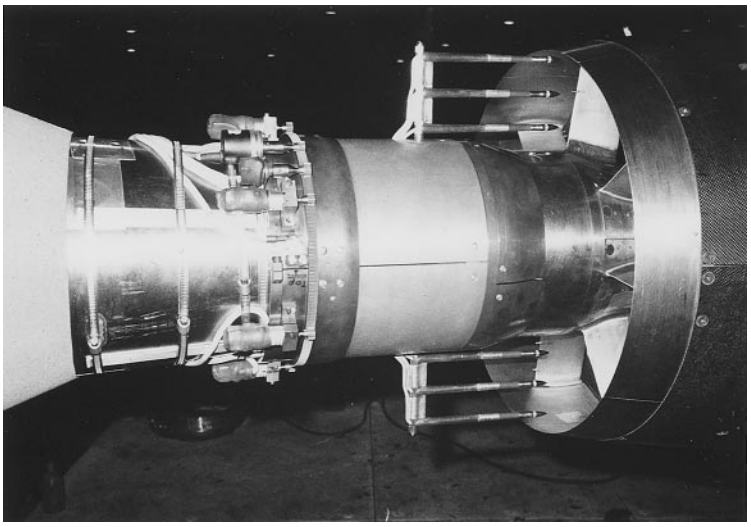

Figure 7. A view of the microphone traversing system mounted on the hub.

microphone signals. The analyzers were triggered by a one-pulse-per-revolution signal to obtain the averaged complex pressure spectra. In this way all non-rotational signal components, such as the turbulent pressure fluctuations of the jet flow, were suppressed. To eliminate leakage effects due to variations of the impeller speed, the sampling frequencies of the FFT analyzers were synchronized with the rotor speed.

The numerical mode analysis used is described in references [1, 2] and can be summarized as follows. As already mentioned, the sound pressure in the exhaust plane can be resolved into circumferential modes $A_m(r_j)$ for each frequency $\omega$ and each circular path with the radial position $r_j$ by using the relation

$$p_{sj} = \sum_{m=-\infty}^{\infty} A_m(r_j) \mathrm{e}^{\mathrm{i}m\varphi_s}. \tag{31}$$

Here the complex quantity $p_{sj}$ describes the measured pressure amplitude and phase at the circumferential positions $\varphi_s$ and the radial position $r_j$. A discrete Fourier-transform with respect to the circumferential angle $\varphi$ was used to determine the complex circumferential modes $A_m(r_j)$ from the circumferential distribution of the complex pressure, for each radial position $r_j$. In this study, the circumferential modes are determined in the range of $m = -59$ to 59 from the 120 complex pressure spectra measured on one circular path.

In a second step the circumferential modes $A_m(r_j)$ are expanded into a series of radial modes with complex amplitudes $A_{mn}$:

$$A_m(r_j) = \sum_{n=0}^{\infty} f_{mn}(\sigma_{mn} r_j/R) A_{mn} \qquad \text{with } f_{mn}(\sigma_{mn} r_j/R) = \mathrm{J}_m(\sigma_{mn} r_j/R) + Q_{mn} \mathrm{Y}_m(\sigma_{mn} r_j/R). \tag{32}$$

Here, $\mathrm{J}_m$ and $\mathrm{Y}_m$ are the Bessel functions of the first and second kind of order $m$, and the eigenvalue $\sigma_{mn}$ and the coefficient $Q_{mn}$ can be determined by using the boundary condition of the rigid wall on the hub and shroud. A linear system of equations was established for each circumferential mode order $m$ and solved by using the least squares fit method. To check the validity of the mode distribution $A_{mn}$ obtained, these radial mode distributions are used to calculate the complex pressure on all measurements points for a comparison

with the measured pressure fluctuations. The differences between the measured and calculated pressures were very small in both amplitude and phase.

### 4.3. FAR FIELD MEASUREMENTS

The arrangement of the propfan model in the open test section of the German–Dutch Wind Tunnel (Deutsch–Niederländischer Windkanal, DNW) is schematically shown in Figure 8. The sound pressure in the acoustic far field was measured with a vertical microphone array, which could be moved parallel to the axis of the propfan model. Acoustic free field conditions are established in the test region due to the acoustic treatment of the walls, and all the other test installations are covered with sound absorbing material. The far field measurements were carried out by Dobrzynski, Gelhar and Böttcher [3] of the DLR-Abteilung Technische Akustik in Braunschweig. The distance of the lateral measurement plane from the rotor axis was 2 m ($10R$). By moving the microphone array in the axial direction, the sound pressure distribution was measured in the polar angle range from $\vartheta = 30^\circ$ to $155^\circ$ in $5^\circ$ increments at all nine microphones of the microphone array. The vertical distances between the microphones were 0·5 m, which corresponds to the circumferential positions $\varphi = -47^\circ$, $-39^\circ$, $-29^\circ$, $-17^\circ$, $-3^\circ$, $11^\circ$, $24^\circ$, $35^\circ$ and $43^\circ$. For the entire traversing range, the microphones, which are fitted with nose cones, are located inside the potential core of the wind tunnel flow to avoid disturbances caused by the shear flow.

## 5. MODE DISTRIBUTIONS IN THE EXIT PLANE

In the following tables and diagrams, the sound pressure level is given in dB relative to an arbitrary reference value. This reference value is kept constant throughout the paper so that data shown in different tables and diagrams can be compared to each other.

During the initial investigations on the propfan model, measurements with different numbers of microphone probes in the jet flow were carried out to check, whether or not the microphones influence the pressure fluctuations in the far field and in the exit plane.

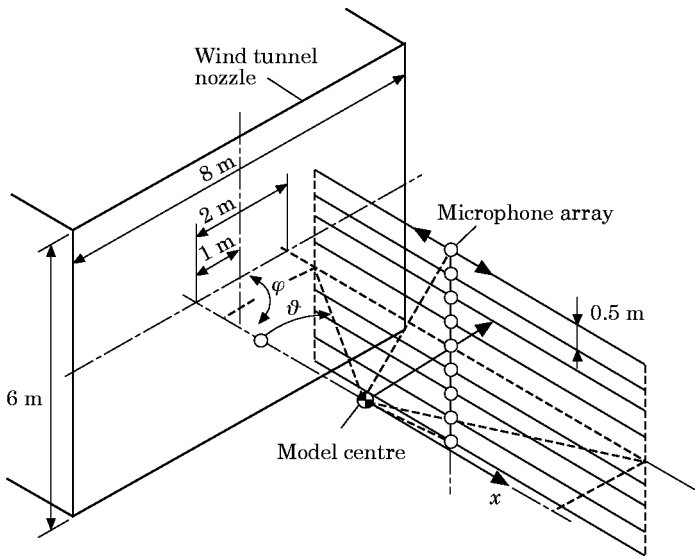


Figure 8. The arrangement of the propfan model and the microphone traversing system in the open test section of the German–Dutch Wind Tunnel (DNW) for the acoustic far field measurements.

The sound spectra measured in the far field with zero, one and four microphones on the hub showed no differences in the sound level for the blade tone and its harmonics. The same result is found by the comparison of the pressure spectra measured at one position in the exit plane with one and all microphones placed in the jet flow. The conclusion of the initial investigation was that the influence of the microphone probes on the pressure fluctuations can be neglected for the tone components, which are the only frequencies considered in this paper. For more details about this investigation, see reference [1].

As an example, a frequency spectrum measured at one circumferential position and averaged in the frequency domain is shown in Figure 9. The blade tone and its harmonics dominate the spectrum. Measurements in the far field carried out by Dobrzynski *et al*. [3] have shown that the second, third and fourth harmonics are mainly responsible for the noise emission of the propfan. For these frequencies typical circumferential mode distributions $|A_m|$ are depicted in Figure 10. The blade stagger angle is the same for both rotors, $\psi = -6^\circ/-6^\circ$, the wind tunnel flow Mach number is $M = 0{\cdot}22$ at zero angle of attack, $\alpha = 0$, and the relative pressure ratio of the fan is $\pi_{rel} = 1$ (operating point 21/02 in Table 1). The mode distributions measured at different radial positions from the axis are labelled by different line symbols, while the various point symbols indicate which interaction mechanism is responsible for the particular circumferential mode. Noise sources are the aerodynamic interaction between the inlet flow and first rotor, the

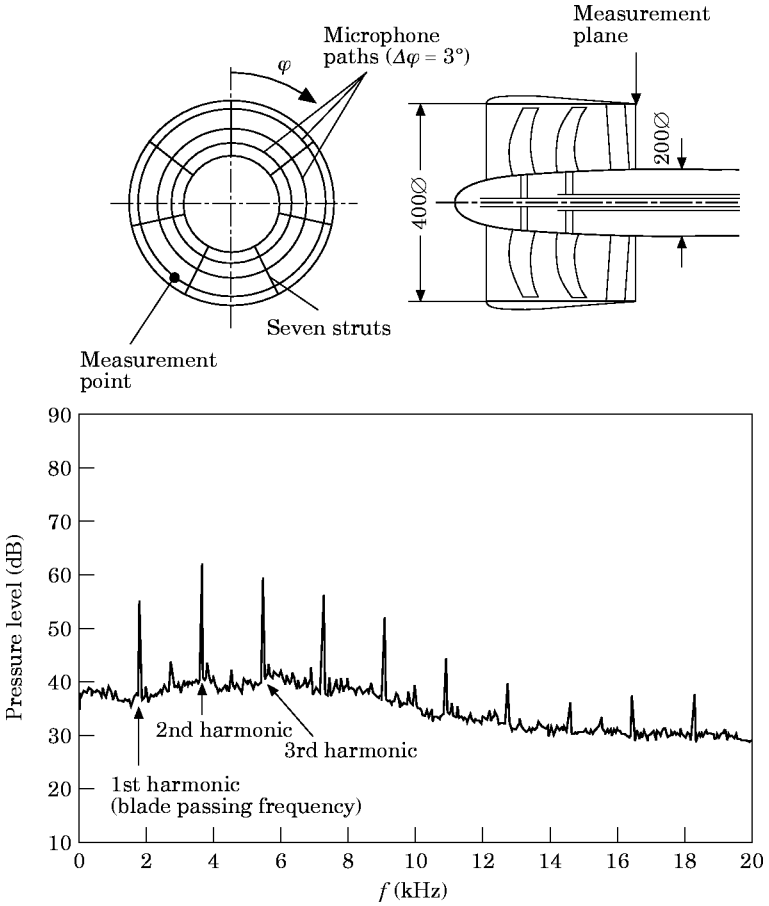


Figure 9. The sound pressure spectrum in the exhaust plane.

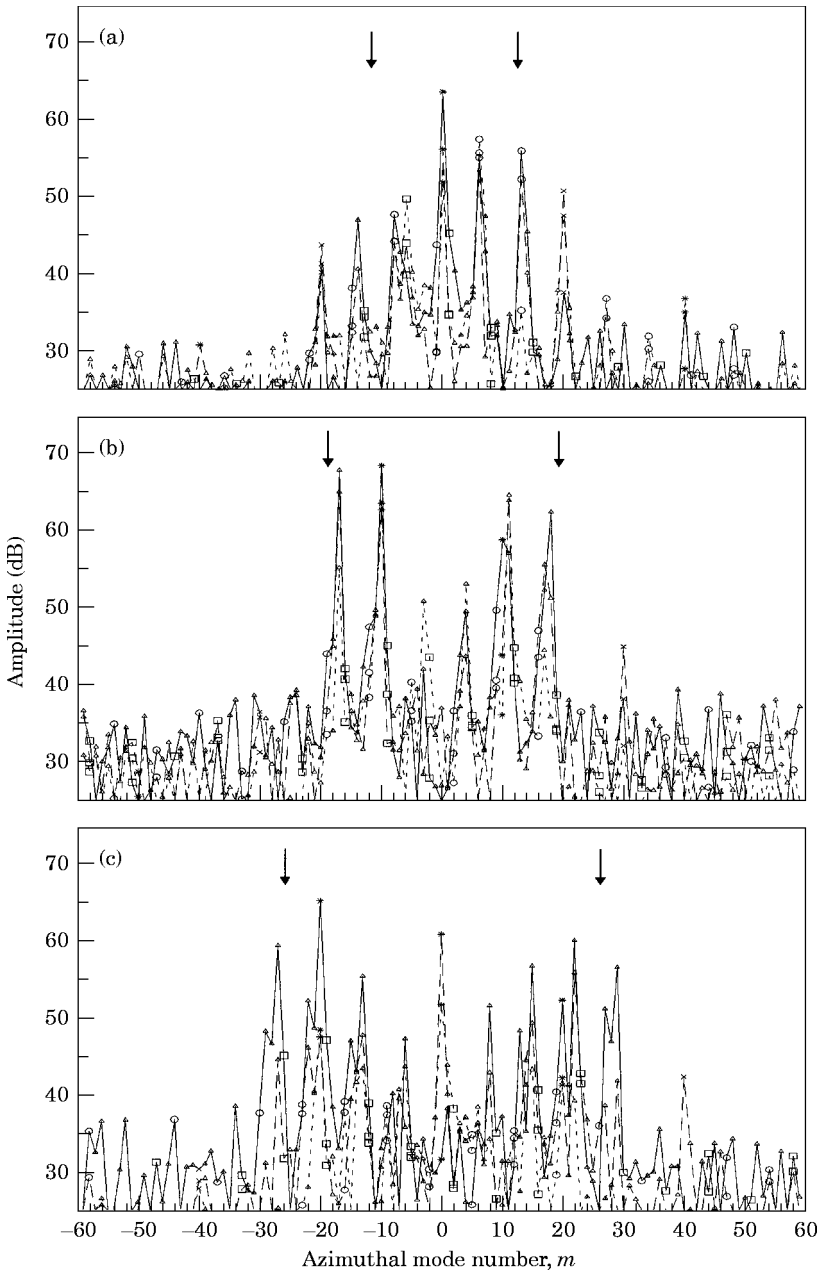


Figure 10. The circumferential mode distribution of the blade tone harmonics 2–4 at maximum thrust. (a) 2 × blade passing frequency; (b) 3 × blade passing frequency. (c) 4 × blade passing frequency. ∗, Rotor 1/rotor 2; ○, rotor 2/struts; □, rotor 1/struts; ×, rotor 1/rotor 2 and rotor 1/struts or rotor 2/struts; △, other modes. ——, $r/R = 0{\cdot}96$; – – –, $r/R = 0{\cdot}785$; ---, $r/R = 0{\cdot}61$. No. 21/02, $\beta = -6^\circ/-6^\circ$, $\pi_{rel} = 1$, $M = 0{\cdot}22$, $\alpha = 0$.

interaction between the two counter-rotating rotors, the interaction between the second rotor and the struts and, finally, the interaction between the wake flow of the first rotor with the struts. Knowing the dominant modes makes it possible to conclude what the main noise generation mechanisms of the propfan model are and this knowledge is helpful for the development of low noise engines; for more details, see references [1, 2]. Two vertical

arrows in each graph mark the range of propagational modes with the mode order $|m|$, 0 ($n = 0$) in the annular cross section of the exit plane. At all operation conditions tested, the dominant circumferential order $|m|$ are very low compared to the modes with high levels. Therefore, one can assume that the amplitudes of all circumferential modes $|m| > 59$ are also very low, so that all dominant modes are not influenced by aliasing effects.

For these dominant circumferential modes $m$, the radial mode amplitudes $A_{mn}$ are calculated from the circumferential mode distributions obtained at different radial positions as described in section 4.2. The maximum number of radial modes, which can be calculated from the experimental data, is equal to the number of circumferential measurement paths spaced over the duct radius. In this study, measurements were performed at three different radial positions and therefore only the radial modes $n = 0$, 1 and 2 could be calculated for each circumferential mode order $m$. As an example, in Table 2 are shown the radial mode distributions of the third harmonic calculated from the circumferential mode distribution depicted in Figure 10: i.e., for the case of maximum thrust with a pressure ratio of $\pi_{rel} = 1{\cdot}0$. An additional mode distribution is shown in Table 3 for the case of middle thrust condition with a pressure ratio of $\pi_{rel} = 0{\cdot}4$ (operating point 21/09 in Table 1). For some of the circumferential modes $m$, not only the radial mode $n = 0$ is found but also the modes $n = 1, 2$, which have sometimes larger amplitudes than the mode $n = 0$. For these circumferential modes, it is quite possible that modes with even higher radial mode order $n$ exist in the exit plane and these modes influence the radial mode analysis (aliasing effect). Additional measurements at other radial positions would be necessary to determine the amplitudes of the modes $n > 2$. During this investigation, measurements at additional radial positions were not possible, and therefore the mode distributions obtained from the three radial positions were used for the calculation of the sound radiation from the exhaust side of the propfan model.

TABLE 2

*The mode distribution of the third blade harmonic in the exit plane at maximum thrust: operating point* 21/02 (*see Table* 1)

| Mode order | | Amplitude | Phase |
|---|---|---|---|
| $m$ | $n$ | (dB) | (degrees) |
| −17 | 0 | 75·1 | −138·2 |
| −17 | 1 | 78·7 | 17·1 |
| −17 | 2 | 55·7 | −44·3 |
| −10 | 0 | 79·5 | 149·1 |
| −10 | 1 | 68·5 | 113·4 |
| −10 | 2 | 66·6 | 136·5 |
| 10 | 0 | 66·4 | 103·8 |
| 10 | 1 | 60·7 | −90·2 |
| 10 | 2 | 55·0 | 68·4 |
| 11 | 0 | 66·3 | −28·8 |
| 11 | 1 | 72·9 | −30·9 |
| 11 | 2 | 72·8 | 55·8 |
| 17 | 0 | 51·3 | 26·1 |
| 17 | 1 | 67·9 | −105·7 |
| 17 | 2 | 46·1 | 178·7 |
| 18 | 0 | 74·2 | 74·5 |
| 18 | 1 | 64·7 | −47·5 |
| 18 | 2 | 40·8 | 123·4 |

TABLE 3

*The mode distribution of the third blade tone harmonic in the exit plane at middle thrust: operating point* 21/09 (*see Table* 1)

| Mode order | | Amplitude | Phase |
|---|---|---|---|
| $m$ | $n$ | (dB) | (degrees) |
| −12 | 0 | 59·6 | 48·3 |
| −12 | 1 | 36·9 | 21·8 |
| −12 | 2 | 32·2 | −8·3 |
| −11 | 0 | 62·9 | 34·8 |
| −11 | 1 | 44·3 | −7·1 |
| −11 | 2 | 33·2 | −98·1 |
| −10 | 0 | 65·6 | 22·6 |
| −10 | 1 | 51·4 | −29·1 |
| −10 | 2 | 40·5 | 163·7 |
| 4 | 0 | 42·6 | −157·6 |
| 4 | 1 | 36·4 | 29·1 |
| 4 | 2 | 34·9 | −126·8 |
| 9 | 0 | 50·4 | −66·7 |
| 9 | 1 | 50·8 | 135·7 |
| 9 | 2 | 35·9 | 72·2 |
| 10 | 0 | 63·2 | 38·5 |
| 10 | 1 | 53·0 | −3·1 |
| 10 | 2 | 29·5 | −161·2 |
| 11 | 0 | 65·4 | 122·7 |
| 11 | 1 | 48·9 | −159·9 |
| 11 | 2 | 37·8 | 60·3 |

## 6. MODEL OF UNIFORM FLOW FIELD

In the first case, a uniform flow field parallel to the rotor axis ($x$-direction) is considered; i.e., the different flow velocities between the jet flow and the external flow are disregarded. As already mentioned, no information about the acoustic parameters on the inlet side of the propfan is known, so that only the sound radiation from the exit plane can be calculated. It is assumed that the shroud is infinitely long on the engine inlet and the hub is never ending on the exhaust side; see Figure 11. In this way one of the acoustical parameters is known over the whole surface, as is required by the equivalent source method, because the normal component of both the particle velocity $v_n$ and the displacement $h_n$ is zero on the rigid wall of the shroud and hub and the pressure fluctuations in the exit plane can be calculated by using the mode distributions obtained from the near field measurements.

### 6.1. CALCULATION PROCESS

In section 2 it was shown that the equivalent sources have to satisfy the boundary conditions over the whole surface, and to prove these conditions the calculation is carried out in four steps at each frequency $\omega$. First, a distribution of ring sources is chosen and, second, for each circumferential mode $m$, the strengths of the ring sources (equivalent sources) are calculated by using the boundary conditions on the surface. In the third step, the pressure distribution in the exit plane and particle displacement $h_n$ on the surface generated by the ring sources are calculated and compared with the actual boundary conditions. If a good agreement is found, then the radiated sound field is calculated in the

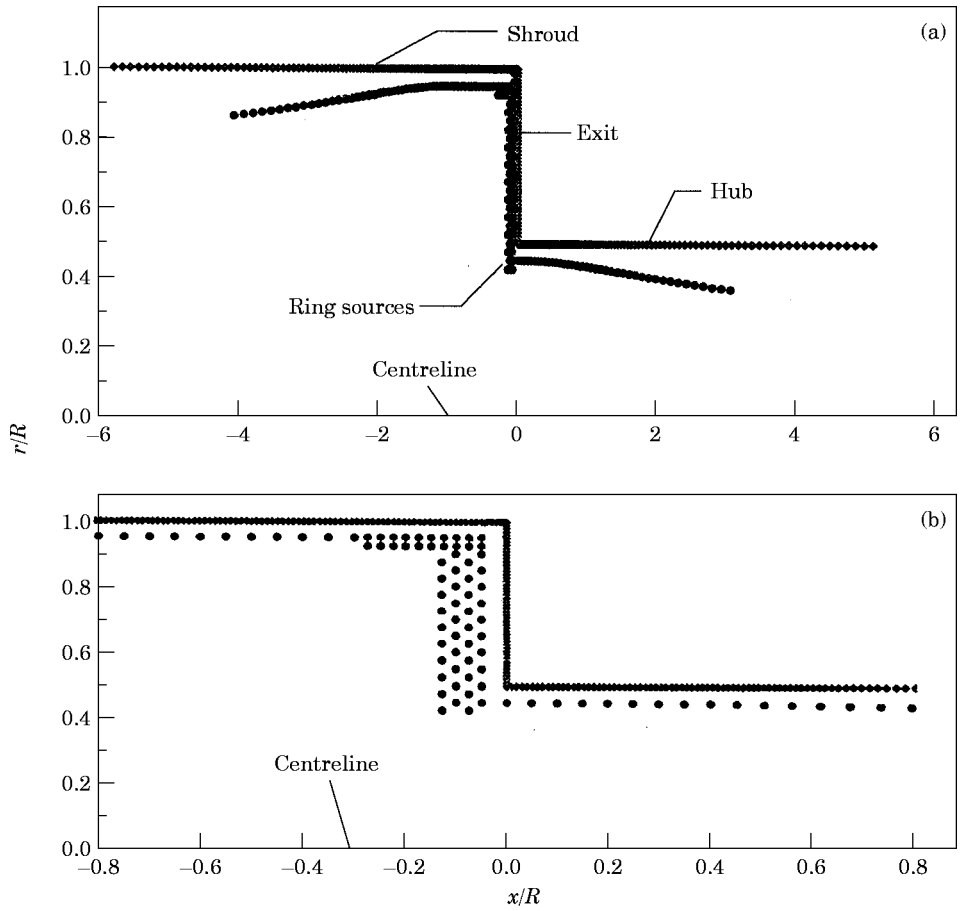


Figure 11. The arrangement of the ring sources and surface points: (a) the total source region; (b) the region near the exit plane enlarged. ●, Ring souce; ◆, surface point.

last step. Otherwise, a new source distribution has to be chosen and the calculation starts at the second step again until the boundary conditions are satisfied.

### 6.2. ARRANGING THE RING SOURCES

It was shown in section 2 that the equivalent sources have to be placed inside of the radiator, but it is not necessary to locate them in the same region as the real sources. During the initial investigations, different arrangements of ring sources are tried for this radiation problem and some of them are discussed in reference [2]. The final arrangement, which satisfies the boundary condition as shown in section 6.3, is shown in Figure 11. The initial investigation showed, that the ring sources in the region around the exit plane have to be placed close to the surface to satisfy the boundary conditions, especially in the corners of the shroud to the exit plane and from the exit plane to the hub. Here, on the one hand, zero particle velocity is required on the shroud and hub but, on the other hand, high particle velocity amplitudes exist in the exit plane, from where the sound field is radiated into the far field. These requirements cannot be fulfilled by using only one source row, because the ring sources radiate in all directions, and the sources in the corners are close to both the exit plane and the wall of the shroud or hub. Thus, additional rows of sources

close to the first row are introduced, so that two adjacent sources can radiate like a dipole to generate a high particle velocity in the axial direction and a low velocity in the radial direction. The sources, which are radiating in such a way, are determined by the least squares fit method, because the method calculates the amplitude and phases of the sources. Also, equivalent sources are placed away from the exit plane to compensate for the particle velocity generated by the sources near the exit plane. During the initial investigation, the best results were obtained when the radii of the ring sources were decreased with their distance from the exit plane. A possible reason for this behaviour is that on the surface away from the exit the wavelength of the normal component of the particle velocity $v_n$ is longer than in the exit region and thus the equivalent sources need a greater distance to the surface to compensate for $v_n$ (rigid wall on the hub and shroud). Finally, the author wishes to mention that it is quite possible that fewer sources could be used to obtain comparably good results, which leads only to a reduction in the necessary computation time and not to an improvement of the accuracy in the calculation.

The total number of sources was $N_q = 156$, and their amplitudes $q_{mj}$ were calculated by applying the boundary conditions formulated in equation (33), for each circumferential mode order $m$. The different sources are distinguished by the index $j = 1, \ldots, N_q$ and the sound radiation of each source is described by $\Pi_{mj}$; see equation (29). The first two equations are derived from equation (9) obtained by considering the rigid surfaces of the shroud and the hub, and the third equation involves the pressure fluctuations in the exit plane:

$$\text{shroud} \quad \sum_{j=1}^{N_q} q_{mj} \frac{\partial \Pi_{mj}}{\partial n} = 0, \qquad \text{hub} \quad \sum_{j=1}^{N_q} q_{mj} \frac{\partial \Pi_{mj}}{\partial n} = 0, \qquad \text{exit} \quad \sum_{j=1}^{N_q} q_{mj} \Pi_{mj} = p_{m_{exit}}. \quad (33)$$

In this investigation the surfaces of the shroud and the hub are parallel to the $x$-axis and, thus, the normal derivative $\partial/\partial n$ is equal to the radial derivative $\partial/\partial r$. $p_{m_{exit}}$ depends on the radius $r$ and is given by a sum over the radial mode distribution $A_{mn}$ determined experimentally; see sections 4.2 and 5:

$$p_{m_{exit}} = \sum_{n=0}^{\infty} f_{mn}(\sigma_{mn} r/R) A_{mn}, \qquad f_{mn}(\sigma_{mn} r/R) = \mathrm{J}_m(\sigma_{mn} r/R) + Q_{mn} \mathrm{Y}_m(\sigma_{mn} r/R). \quad (34)$$

For the calculation the surface is divided into $N_s = 565$ elements in the range $x = -6R$ to 0 on the shroud, over the exit plane, and over the hub in the range $x = 0$ to $5R$; see Figure 11. The distances between the surface points (96 elements per radius $R$) were equidistant in the exit plane as well as on the shroud and hub in the region near the exit. To limit the number of surface elements, the distance between the surface points increases as the axial distance from the exit grows. By using equations (33) and (34), one obtains an over-determined linear system of size $N_s \times N_q$, which is solved by using the least squares fit method.

### 6.3. VERIFICATION OF THE RING SOURCE DISTRIBUTION

As an example, the calculated radial pressure distribution in the exit plane and the displacement on the shroud are compared to the actual boundary conditions in Figures 12 and 13, respectively, for the third blade tone harmonic at the opening point 21/09; compare with Table 1. The radial mode distribution $A_{mn}$ used for the calculation is given in Table 3 and the Mach number $M$ is 0·43. In Figure 12 the full line represents the radial pressure

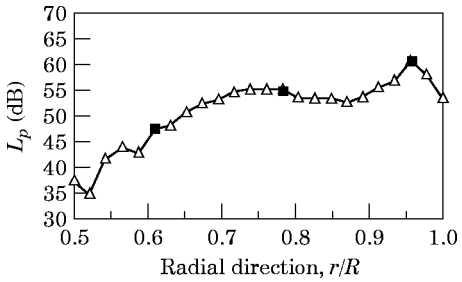


Figure 12. The predicted (—△—) and measured (■) pressures of the third blade tone harmonic ($kR = 14{\cdot}4$) in the exit plane ($\varphi = 0$); uniform flow model ($M = 0{\cdot}43$); operatoing point 21/09 (see Table 1).

distribution generated by the equivalent sources at the circumferential angle $\varphi = 0$ and the pressure levels measured at three radial positions are depicted by square symbols. Very good agreement is obtained. In Figure 13 is shown the particle displacement (see equation (9)) produced by the equivalent sources over the whole surface $z$ at the circumferential angle $\varphi = 0$. The variable $z$ goes along the surface of the propfan and is zero in the corner shroud/exit plane. $z < 0$ denotes the shroud ($x < 0$), $0 < z < 0{\cdot}5$ represents the exit plane ($x = 0$), and on the hub ($x > 0$) $z$ is greater than 0·5. The particle displacement on the shroud and the hub is more than 20 dB lower than that at the exit plane and does not contribute to the radiated sound field. Similar results are found at other circumferential positions, and the conclusion is that the ring source distribution chosen satisfies the boundary condition over the entire surface and can, therefore, be used to calculate the radiated sound field, as was shown in Section 2.

### 6.4. COMPARISON OF CALCULATED AND MEASURED SOUND RADIATION

For different frequencies and operating conditions of the propfan model, comparisons are carried out between the measured and calculated sound pressure on a lateral plane in the far field. The position of the lateral plane relative to the propfan model is shown in Figure 8 and the sound pressure measurements are described in section 4.3. As an example, in Figure 14 are compared the 3-D plots of the measured predicted sound pressures of the third blade tone harmonic in the lateral measurement plane. The same data are depicted in Figure 15 as contour plots, to give a better comparison of the directivity characteristics. In both figures the grey scale denotes the sound pressure levels in 5 dB steps. At the

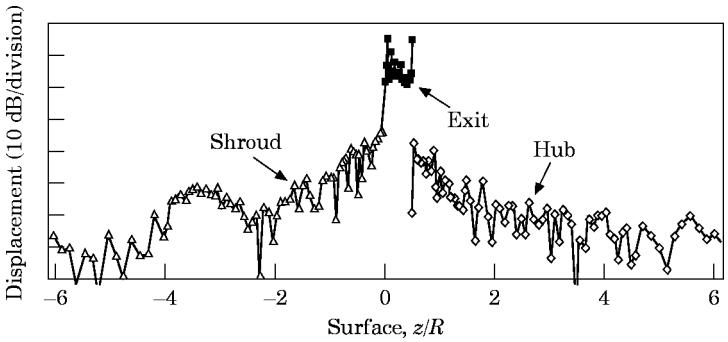


Figure 13. The particle displacement of the third blade tone harmonic ($kR = 14{\cdot}4$) on the surface of the propan ($\varphi = 0$); uniform flow model ($M = 0{\cdot}43$); operating point 21/09 (see Table 1). —△—, shroud; —■—, exit; —◇—, hub.

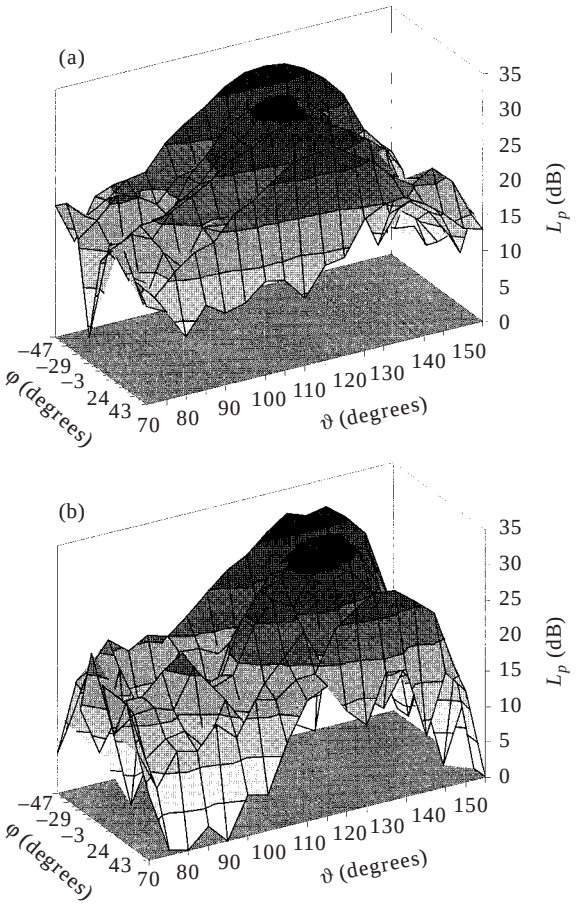


Figure 14. The measured (a) and predicted (b) sound pressures of the third blade tone harmonic ($kR = 14{\cdot}4$) in a plane lateral to the propfan; uniform flow model ($M = 0{\cdot}43$); operating point 21/09 (see Table 1).

operating point 21/09, the non-dimensional frequency of the third harmonic was $kR = 14{\cdot}4$ and the Mach number of the wind tunnel flow $M = 0{\cdot}22$. For the calculations, a uniform flow around the propfan model was assumed with the Mach number $M = 0{\cdot}43$, which is that of the jet flow.

Good agreement is observed between the maximum sound pressure levels, the general shape of the radiation characteristics, and the circumferential location of the region of maximum sound pressure level described by the angle $\varphi$. However, the contour plots reveal that the predicted polar location (angle $\vartheta$) of the maximum sound pressure level is shifted by about 10°–20° in the direction of flow compared to the measured ones. This discrepancy is believed to be caused by the assumption of uniform flow conditions in the entire sound field, because the lower Mach number $M = 0{\cdot}22$ of the wind tunnel flow was disregarded at the calculations.

The knowledge of the directivity characteristic is necesary for an accurate prediction of flyover levels and the noise level in the neighbourhood of airports. To improve the sound field prediction based on measured near field data, one has to consider the different velocities in the jet flow and in the flow external of the aircraft engine.

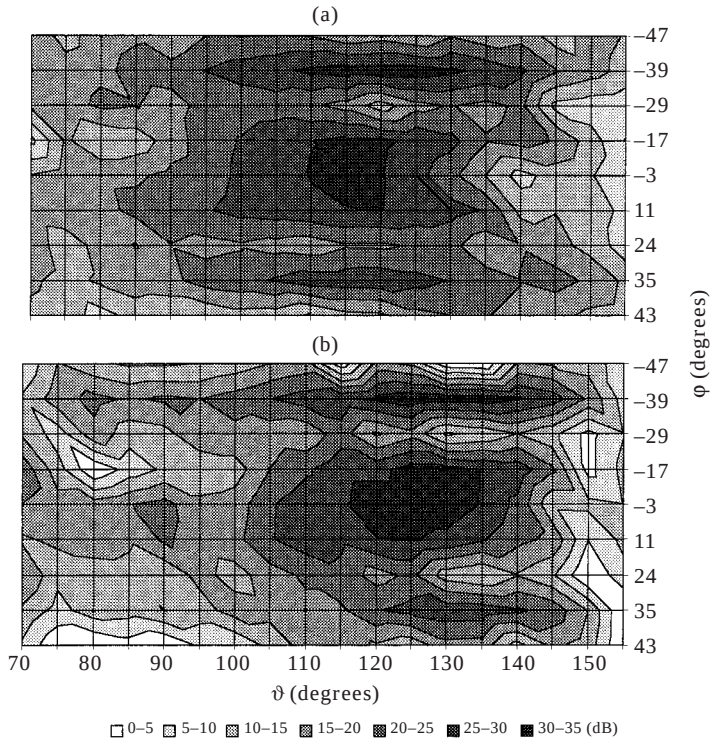


Figure 15. Contour plots of the measured (a) and predicted (b) sound pressures of the third blade tone harmonic ($kR = 14{\cdot}4$) in a plane lateral to the propfan; uniform flow model ($M = 0{\cdot}43$); operating point 21/09 (see Table 1).

## 7. CONSIDERATION OF THE DIFFERENT FLOW VELOCITIES IN THE JET AND THE WIND TUNNEL FLOW

To consider approximately the non-uniform flow conditions around the propfan model, the sound field is divided into two regions with different uniform flow velocities, as is shown in Figure 16. In region B1 the Mach number is assumed to be equal to that of the jet exit flow, and in region B2 it is equal to the wind tunnel flow velocity. These different Mach numbers mean that two independent sets of equivalent sources are necessary to describe the sound field in the two regions, because the radiation function $\Pi_m$ of the ring sources applies to a uniform flow field with the Mach number $M$; see equation (29).

### 7.1. ARRANGING THE RING SOURCES

Two different sets of equivalent sources $q_{mj}^{\mathrm{B1}}$ and $q_{ml}^{\mathrm{B2}}$ are used to describe the sound field in the regions B1 and B2; see Figure 16. The sources $q_{mj}^{\mathrm{B1}}$ are located around the region B1, and accordingly, for the sound field in region B2, the sources $q_{ml}^{\mathrm{B2}}$ are used and located outside of B2. By using the radiation functions $\Pi_{mj}^{\mathrm{B1}}$ and $\Pi_{ml}^{B2}$ one obtains, for the sound pressures in the regions B1 and B2, respectively

$$p_m^{\mathrm{B1}} = \sum_{j=1}^{N_q^1} q_{mj}^{\mathrm{B1}} \Pi_{\mathrm{mj}}^{\mathrm{B1}}, \qquad p_m^{\mathrm{B2}} = \sum_{\ell=1}^{N_q^2} q_{m\ell}^{\mathrm{B2}} \Pi_{\mathrm{m}\ell}^{\mathrm{B2}}. \tag{35}$$

$\Pi_{mj}^{\mathrm{B1}}$ is the radiation function of the $j$th source for the region B1 with the Mach number of the jet flow (see equation (29)), and $\Pi_{m\ell}^{\mathrm{B2}}$ is the radiation function of the $\ell$th source for

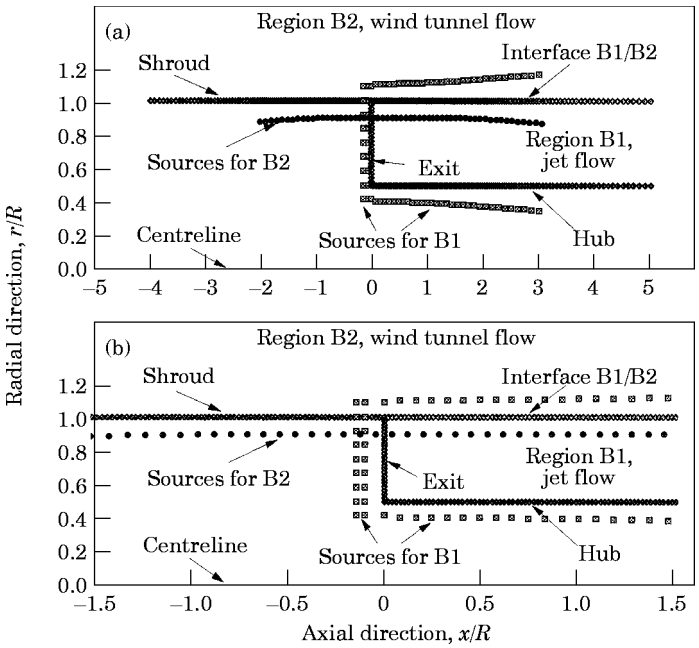


Figure 16. The arrangement of the ring sources and surface points: (a) total source region; (b) region near the exit plane ($x/R = -1{\cdot}5$ to $1{\cdot}5$) enlarged. ◆, Hub; ◇, shroud; ◆, exit; ◇, B1/B2. □, sources B1; ●, sources B2.

the region B2 with the Mach number of the wind tunnel flow. $N_{q^1} = 82$ sources are used to describe the sound field in region B1 and $N_{q^2} = 58$ sources for region B2. Similar to the calculation in section 6.2, two rows of ring sources with a separation distance of $\frac{1}{10}$ of the wavelength are placed before the exit plane outside of B1. In this way, the sources can radiate like dipoles which generate large acoustic velocity component in the axial direction but only a small radial component on the hub.

The boundary conditions formulated by equations (36) and (37) are used to determine the strengths of the sources. As before, the first two of the following three equations are obtained by considering the rigid walls of the shroud and the hub, where the normal derivative of the pressure vanishes, and the third equation results from the condition that the equivalent ring sources $q_{mj}^{\mathrm{B1}}$ have to approximate the measured pressure fluctuations in the exit plane for each mode order $m$:

$$\text{shroud} \quad \sum_{\ell=1}^{N_q{}^2} q_{m\ell}^{\mathrm{B2}} \frac{\partial \Pi_{m\ell}^{\mathrm{B2}}}{\partial n} = 0, \qquad \text{hub} \quad \sum_{j=1}^{N_q{}^1} q_{mj}^{\mathrm{B1}} \frac{\partial \Pi_{mj}^{\mathrm{B1}}}{\partial n} = 0, \qquad \text{exit} \quad \sum_{j=1}^{N_q{}^1} q_{mj}^{\mathrm{B1}} \Pi_{mj}^{\mathrm{B1}} = p_{m_{exit}}. \tag{36}$$

The normal derivative $\partial/\partial n$ is equal to the radial derivative $\partial/\partial r$ in this investigation, because the surfaces of the shroud and hub are parallel to the $x$-axis. $p_{m_{exit}}$ is calculated from the radial mode distribution determined experimentally by using equation (34). The surface velocities on the shroud and the hub are generated by the source terms $q_{m\ell}^{\mathrm{B2}}$ and $q_{mj}^{\mathrm{B1}}$, respectively.

Two additional relations are derived by matching the acoustic pressure $p$ and particle displacement $h_n$ at the interface between the regions B1 and B2. Here, the pressure fluctuations in both regions must be equal, and the same is required for the

normal component of the displacement $h_n$; for more details see references [17, 23]. One obtains

$$\text{interface B1/B2, pressure } p, \qquad \sum_{\ell=1}^{N_q{}^2} q_{m\ell}^{\mathrm{B2}} \Pi_{m\ell}^{\mathrm{B2}} = \sum_{j=1}^{N_q{}^1} q_{mj}^{\mathrm{B1}} \Pi_{mj}^{\mathrm{B1}},$$

$$\text{interface B1/B2, displacement } h_n, \qquad \sum_{\ell=1}^{N_q{}^2} q_{m\ell}^{\mathrm{B2}} \frac{\partial \Pi_{m\ell}^{\mathrm{B2}}}{\partial n} = \sum_{j=1}^{N_q{}^1} q_{mj}^{\mathrm{B1}} \frac{\partial \Pi_{mj}^{\mathrm{B1}}}{\partial n}, \tag{37}$$

where an approximate relation is used for the particle displacement $h_n$ in the normal direction, which is obtained by using the following consideration. For harmonic motions the convective Euler equation and the total derivative of the displacement $h_n$ is given by

$$-\mathrm{i}\omega v_n + U\,\partial v_n/\partial x = -(1/\rho)\,\partial p/\partial n, \qquad v_n = -\mathrm{i}\omega h_n + U\,\partial h_n/\partial x, \tag{38}$$

which leads to

$$h_n = \frac{1}{\rho\omega^2}\frac{\partial p}{\partial n} - \mathrm{i}2\,\frac{M}{k}\frac{\partial h_n}{\partial x} + \frac{M^2}{k^2}\frac{\partial^2 h_n}{\partial x^2}. \tag{39}$$

Equation (38) reveals that there is a discontinuity of the acoustic velocity $v_n$ at the interface between regions B1 and B2 if the flow velocities $U$ in the two regions are different. Introducing the first and second derivatives of $h_n$ with respect to the axial direction,

$$\frac{\partial h_n}{\partial x} = \frac{1}{\rho\omega^2}\frac{\partial^2 p}{\partial n\,\partial x} - \mathrm{i}2\,\frac{M}{k}\frac{\partial^2 h_n}{\partial x^2} + \frac{M^2}{k^2}\frac{\partial^3 h_n}{\partial x^3}, \qquad \frac{\partial^2 h_n}{\partial x^2} = \frac{1}{\rho\omega^2}\frac{\partial^3 p}{\partial n\,\partial x^2} - \mathrm{i}2\,\frac{M}{k}\frac{\partial^3 h_n}{\partial x^3} + \frac{M^2}{k^2}\frac{\partial^4 h_n}{\partial x^4}, \tag{40, 41}$$

into equation (39), one arrives at the following series approximation

$$h_n = \frac{1}{\rho\omega^2}\frac{\partial p}{\partial n} - \frac{\mathrm{i}2}{\rho\omega^2}\frac{M}{k}\frac{\partial^2 p}{\partial n\,\partial x} - \frac{3}{\rho\omega^2}\frac{M^2}{k^2}\frac{\partial^3 p}{\partial n\,\partial x^2} - \mathrm{i}4\frac{M^3}{k^3}\frac{\partial^3 h_n}{\partial x^3} - \ldots, \tag{42}$$

in which the exponent of the Mach number increases from term to term. Since only subsonic flows ($M < 1$) are considered here, the terms involving very high Mach number exponents can be neglected. It is difficult to estimate the contribution of the second, third and the next higher terms on the particle displacement, because of the complicated derivatives of the pressure $p$; see equation (28) and (29). However, it is very likely that the first term in expression (42) dominates, because this term describes the no flow case ($M = 0$) and the influence on the displacement $h_n$ caused by the flow is given by the higher terms. Here, the particle displacement $h_n$ is approximated by

$$h_n \approx (1/\rho\omega^2)\,\partial p/\partial n, \tag{43}$$

and used in the boundary conditions formulated in equations (37). The influence of the flow on the particle displacement $h_n$ is considered only in the radiation functions $\Pi_{mj}^{\mathrm{B1}}$ and $\Pi_{m\ell}^{\mathrm{B2}}$ described in equation (29).

In analogy to section 6.2, the surface of the propfan model and the interface are divided into $N_s = 566$ elements. $N_s$ is greater than the number of sources ($N_{q^1} + N_{q^2} = 140$) and a system of equations, which is solved numerically by using the least squares fit method, could be set up by using equations (36) and (37).

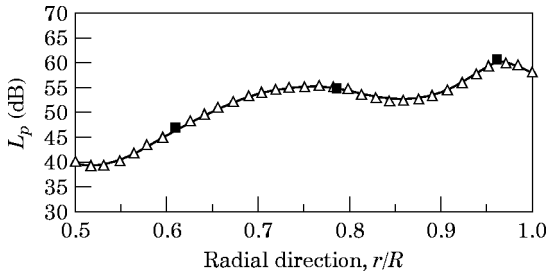


Figure 17. The predicted (—△—) and measured (■) pressure of the 3rd blade tone harmonic ($kR = 14{\cdot}4$) in the exit plane ($\varphi = 0$); non-uniform flow model (jet flow $M = 0{\cdot}43$, wind tunnel flow $M = 0{\cdot}22$); operating point 21/09 (see Table 1).

### 7.2. VERIFICATION OF THE CALCULATION METHOD

As before, in the uniform flow case, the suitability of a given source distribution to accurately predict the sound field of the propfan model is tested by examining how well the boundary conditions at the shroud, at the hub, in the exit plane and at the interface B1/B2 are fulfilled. As an example, the calculated radial pressure distribution of the third blade tone harmonic in the exit plane ($\varphi = 0$) is compared in Figure 17 with the experimental data obtained at three radial positions. The operating condition of the propfan model is 21/09 (see Table 1), and the radial mode distribution used for the calculation is given in Table 3. Very good agreement is found. In Figure 18 is shown for the same case, the acoustic particle displacement produced by the equivalent sources (see equation (9)) at the shroud, the hub, the exit plane and, also, at the interface between the regions B1 and B2. Again, the particle displacement on the shroud and hub turns out to be much lower than in the exit plane, and thus its influence on the radiated sound field can be neglected. The particle displacement at the interface B1/B2 as generated by the two different sets of ring sources in the two regions is indicated by two different point symbols. The agreement between the results is very good, and the same is true for acoustic pressure on the interface which is not shown in the diagram. From the above results one concludes that the ring source distribution chosen satisfies the boundary conditions (36) and (37) over the entire surface and can, therefore, be used to calculate the far field sound pressure.

### 7.3. COMPARISON BETWEEN THE CALCULATED AND MEASURED SOUND RADIATION

Three-dimensional plots and contour plots of the measured and predicted sound fields at the third blade tone harmonic are compared in Figures 19 and 20 for the operating condition 21/09, and in Figures 21 and 22 for the operating condition 21/02; compare with

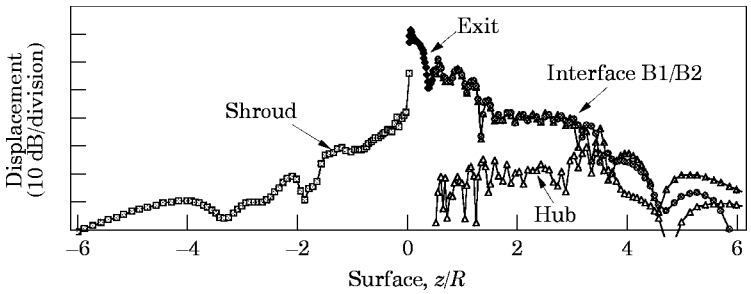


Figure 18. The particle displacement of the third blade tone harmonic ($kR = 14{\cdot}4$) on the surface of the propfan model ($\varphi = 0$); non-uniform flow model (jet flow $M = 0{\cdot}43$, wind tunnel flow $M = 0{\cdot}22$); operating point 21/09 (see Table 1). —△—, Hub; —□—, shroud; —◆—, exit. —▲—, B1; —○—, B2.

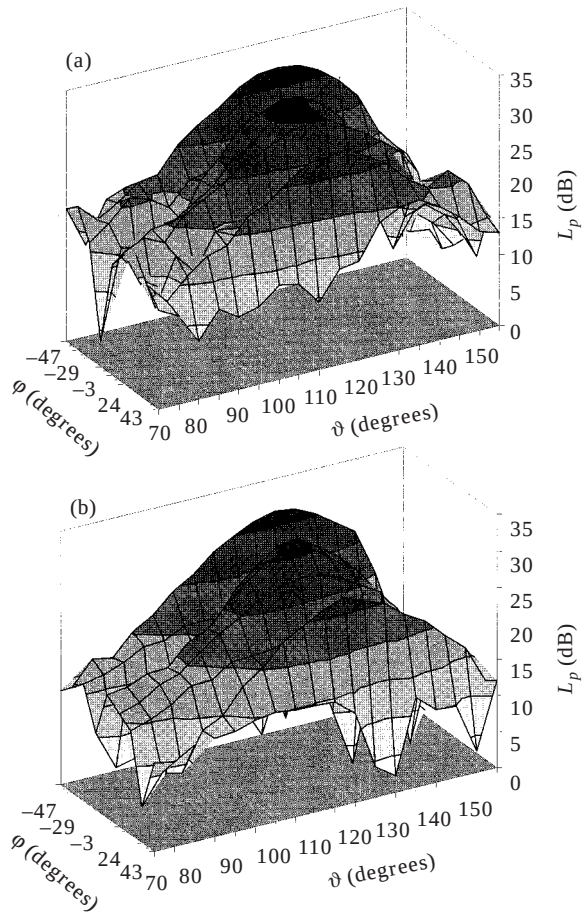


Figure 19. The measured (a) and predicted (b) sound field of the third blade tone harmonic ($kR = 14{\cdot}4$) in a plane lateral to the propfan; non-uniform flow model (jet flow $M = 0{\cdot}43$, wind tunnel flow $M = 0{\cdot}22$); operating point 21/09 (see Table 1).

Table 1. Again, the grey scale in all figures denotes the sound pressure levels in 5 dB steps. The radial mode distributions used for the calculations are given in Tables 2 and 3. At the operating point 21/09, the non-dimensional frequency of the third harmonic is $kR = 14{\cdot}4$ and the relative pressure ratio is $\pi_{rel} = 0{\cdot}4$ (medium thrust), and at the operating point 21/02 the corresponding figures are $kR = 21{\cdot}3$ and $\pi_{rel} = 1{\cdot}0$ (full thrust). At both operating conditions the wind tunnel flow Mach number is $M = 0{\cdot}22$, and the Mach numbers of the jet flow are $M = 0{\cdot}43$ and $0{\cdot}61$.

Very good agreement is found between calculation and measurement in the maximum sound levels, as well as in the radiation characteristics. At the medium thrust condition, the experimental maximum sound level is about 1 dB higher than the predicted level (compare Figures 19 and 20) and a larger difference of about 3 dB is observed at the maximum thrust condition (compare Figures 21 and 22). In the latter case, the velocity difference between the jet flow and the external flow was the largest of all operating conditions tested. The level differences observed in the polar angle range $\vartheta = 70^\circ$–$90^\circ$ are presumably caused by the influence of the sound radiation from the inlet side, which is not accounted for in the present calculations. As an improvement to the uniform flow case

discussed in section 6.4, the agreement between the predicted and measured characteristics is much better in the non-uniform flow case, for both operating conditions, as can be seen in the contour plots depicted in Figures 20 and 22. The locations of the regions with the highest sound levels are the same, with respect to the circumferential angle $\varphi$ as well as the polar angle $\vartheta$. The size of these regions is somewhat smaller in the predicted fields, which is due to the lower calculated sound levels.

Similar results were found at other operating conditions of the propfan and at other harmonics. The results are summarized in Figure 23, where the sound power radiated through the lateral measurement plane ($\vartheta = 70^\circ$ to $155^\circ$ and $\varphi = -47^\circ$ to $43^\circ$) is plotted for the second, third and fourth harmonics and for five different operating points of the propfan. The sound powers were determined under the assumption of acoustic free field conditions: i.e., by integrating the acoustic intensity $I = pv$ over the measurement plane with $v = p/(\rho a)$. $\rho$ is the density of the wind tunnel flow. This equation is valid only in the acoustical and geometrical far field, and it was shown in reference [3] that these conditions are met in the lateral measurement plane for the regions of high sound levels. By dividing the lateral plane into small sections $A_j$ around the $j$th measurement point and by considering the normal vector one obtains for the sound power

$$L_w = 10 \log \left\{ \sum_{j=1}^{N_{mp}} 10^{Lp_j/10} A_j \sin(\vartheta_j) \cos(\varphi_j) \right\}. \tag{44}$$

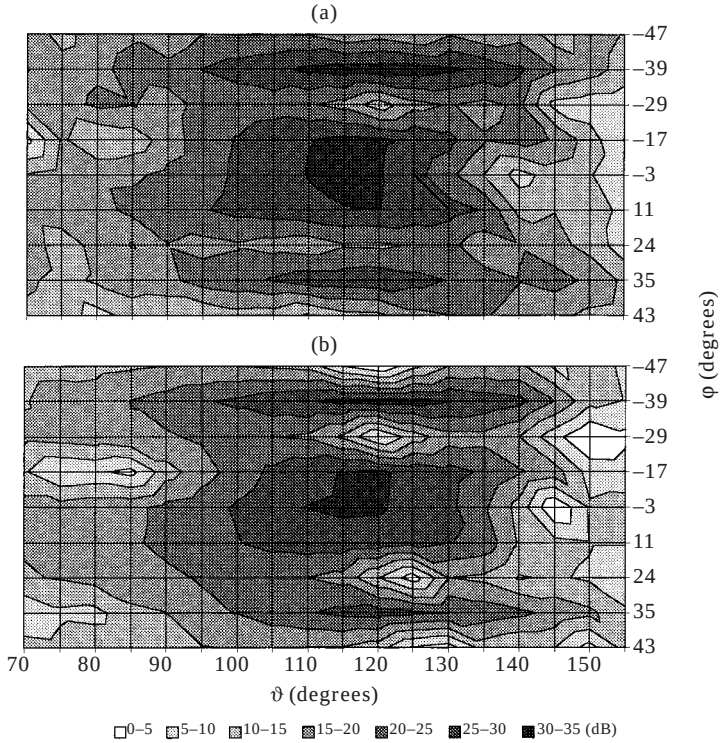


Figure 20. Contour plots of the measured (a) and predicted (b) sound fields of the third blade tone harmonic ($kR = 14{\cdot}4$) non-uniform flow model (jet flow $M = 0{\cdot}43$, wind tunnel flow $M = 0{\cdot}22$); operating point 21/09 (see Table 1).

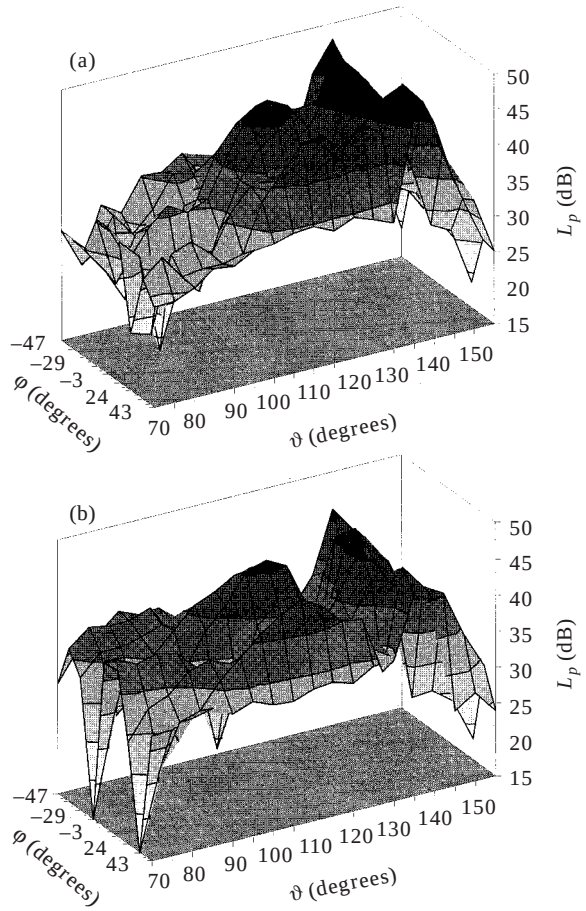


Figure 21. The measured (a) and predicted (b) sound fields of the third blade tone harmonic ($kR = 21{\cdot}3$) in a plane lateral to the propfan; non-uniform flow model (jet flow $M = 0{\cdot}61$, wind tunnel flow $M = 0{\cdot}22$); operating point 21/02 (see Table 1).

$L_{pj}$ denotes the measured or calculated sound pressure level at the $j$th measurement point and $\vartheta_j$ and $\varphi_j$ represent the angles of the normal vector to the lateral plane. $N_{mp}$ is the number of measurements points in the plane.

The comparison presented in Figure 23 covers a range of jet flow Mach numbers from 0·43 to 0·61, two wind tunnel speeds of $M = 0{\cdot}15$ and 0·22, and two blade stagger angles $\beta = -6^\circ/-6^\circ$ and $-8^\circ/-8^\circ$. The lowest non-dimensional frequency considered is $kR = 9{\cdot}6$ (second harmonic, middle thrust), and the highest non-dimensional frequency $kR = 28{\cdot}3$ occurred at the fourth harmonic (maximum thrust). As a consequence of this variation of operating conditions, different sets of acoustic modes are excited in the exit plane of the propfan, as was shown in Tables 2 and 3 for two operating points. Mode distributions at other operating conditions are given in references [1, 2]. The level differences between different operating conditions reflect the influence of the performance (relative pressure ratio $\pi_{rel}$, thrust) of the propfan on the radiated sound power. In Figure 23 very good agreement is shown between the calculated and measured sound power for all three blade tone harmonics and at all operating conditions considered. The

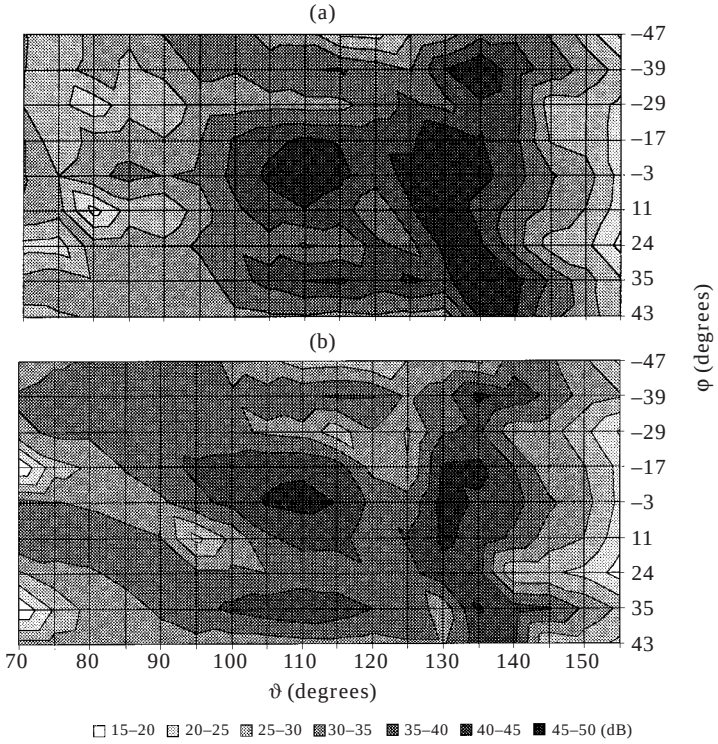


Figure 22. Contour plots of the measured (a) and predicted (b) sound fields of the third blade tone harmonic ($kR = 21{\cdot}3$) non-uniform flow model (jet flow $M = 0{\cdot}61$, wind tunnel flow $M = 0{\cdot}22$); operating point 21/02 (see Table 1).

calculated sound power levels are about 1–3 dB lower than the measured levels. Possible reasons for these small deviations are discussed in the conclusions.

## 8. CONCLUSIONS

A theoretical/numerical approach has been shown, which allows one to predict the radiated sound field of an aircraft engine based on the pressure fluctuations measured in

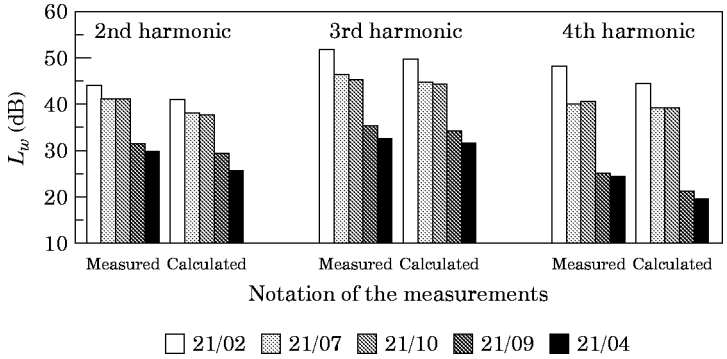


Figure 23. Comparisons of the calculated and measured sound power radiated through the lateral measurement plane in the far field for the second, third, and fourth harmonics under five different operating conditions.

the near field. The method was tested on a propfan model, which was installed in the open test section of the German–Dutch Wind Tunnel. The sound field radiated from the exhaust side was calculated by using the pressure fluctuations measured in the exit plane and compared with the results of acoustic far field measurements. The approach is based on the equivalent source method, which is extended to include the effects of the mean flow of the propfan. In the first calculation model a uniform flow is assumed around the propfan model; i.e., the different flow speeds of the jet flow and wind tunnel flow are neglected. Comparison between the calculated and measured sound radiation showed good agreement in the maximum sound pressure level, but differences are found in the radiation characteristics; these are mainly caused by the different velocities of the jet and the external flow.

In the second model, the non-uniform flow conditions of the propfan were approximately accounted for by dividing the total sound field into two regions with two different flow velocities. A good agreement was found between the predicted and measured radiation characteristics and absolute sound pressure levels. The predicted maximum sound levels are by about 1–3 dB lower than measured ones. Comparisons between predicted and measured sound fields are shown for different blade tone harmonics and operating conditions of the propfan model, which correspond to different flight situations. The differences in the predicted and measured sound power levels radiated through a plane lateral to the rotor axis were about 1–3 dB. In the following, possible reasons for these small deviations are given, which can be used for an improvement of the calculation method:

(i) For the calculation of the particle displacement at the interface between the jet flow and the wind tunnel flow, an approximate equation of the zeroth order was used; compare with equation (43). By considering the terms of higher order in equation (42), a more accurate assessment of the particle displacement can be attained. On the other hand, it is well possible that the approximation used provided a better description of the sound radiation through the shear flow than the exact solution, which implies a sudden change of the flow Mach number at the interface which would cause sound reflections and refractions.

(ii) The shear layer flow between the jet flow and external flow is neglected. By introducing a third region with uniform flow, with a Mach number equal to the average of the jet flow and the external flow, a better description of the sound radiation through a shear flow may possibly be achieved.

(iii) A uniform flow profile was assumed in the exit plane.

(iv) The radial modes $n$ are calculated by using the pressure fluctuations measured at only three different radial positions, which limits the highest radial mode order to be determined to $n = 2$. Very likely, modes of higher radial order $n$ exist in the exit plane, which are not considered in the calculation.

(v) The sound radiation from the inlet side of the propfan model was not included because no experimental near field data were available. The prediction method can also be applied to the inlet side of an aircraft engine with a suitable consideration of the non-uniform flow conditions, similar to the exhaust side.

Finally, the method presented here was developed and tested on a propfan model. However, it is also applicable to other types of aircraft engines. Moreover, the equivalent source method in general can, in principle, be used to describe other radiation problems with arbitrary geometries.

## ACKNOWLEDGMENTS

The author is grateful for discussions with Professor A. Michalke at the Technical University in Berlin and with his colleagues at the DLR in Berlin. Thanks are also due to the DLR in Braunschweig for supplying the far field sound pressure spectra. Special thanks go to Professor G. H. Koopmann and Dr J. B. Fahnline at the Center for Acoustic and Vibration of the Penn State University, where the main part of this work was carried out.

## REFERENCES

1. F. Holste and W. Neise 1992 14*th Aeroacoustic Conference* 1992 *DGLR/AIAA* 92-02-138, 826–835. Experimental determination of the main noise sources in a propfan model by analysis of the acoustic spinning modes in the exit plane.
2. F. Holste 1995 *Dissertation*, *TU Berlin*, *Reihe* 7, *No*. 272. Düsseldorf: VDI-Verlag. Ermittlung der aerodynamischen Lärmquellen und Berechnung des abgestrahlten Schallfeldes mittels der im Nahfeld gemessenen Druckschwankungen am Beispiel eines Triebwerksmodells.
3. W. Dobrzynski, B. Gehlhar and J. Böttcher 1992 14*th Aeroacoustic Conference* 1992 *DGLR/AIAA* 92-02-136, 816–826. Aeroacoustic wind tunnel testing of a counter-rotating shrouded propfan-model.
4. D. G. Crighton 1992 *Mordern Methods in Analytical Acoustics*. London: Springer-Verlag.
5. G. H. Koopmann, L. Sohn and J. B. Fahnline 1989 *Journal of Acoustical Society of America* **86**, 2433–2438. A method for computing acoustic fields based on the principle of wave superposition.
6. T. M. Tomilina 1989 *Soviet Physics—Acoustics* **35**(1), 73–75. Radiation impedance of a hollow cylindrical radiator.
7. L. Cremer 1984 *Acustica* **55**, 44–46. Die Synthese des Schallfeldes eines beliebigen festen Körpers in Luft mit beliebiger Schnelleverteilung aus Kugelschallfeldern.
8. L. Cremer and M. Wang 1988 *Acustica* **65**, 53–74. Die Synthese eines von einem beliebigem Körper in Luft erzeugten Feldes aus Kugelschallfeldern und deren Realisierung in Durchrechnung und Experiment.
9. J. B. Fahnline 1993 *Ph.D Thesis*, *Pennsylvania State University*. The generalized inverse source method for the computation of acoustic fields.
10. M. Heckl 1989 *Acustica* **68**, 251–257. Bemerkung zu Berechnung der Schallabstrahlung nach der Methode der Kugelfeldsynthese (Cremer-Methode).
11. M. Ochmann 1995 *Acustica* **81**, 512–527. The source simulation technique for acoustic radiation problems.
12. A. Boag et al. 1988 *Journal of the Acoustical Society of America* **83**(1), 1–8. Analysis of acoustic scattering from fluid cylinders using a multifilament source model.
13. Y. L. Bobrovnitskii and T. M. Tomilina 1990 *Soviet Physics–Acoustics* **36**(2), 334–338. Calculation of radiation from finite elastic bodies by the method of auxiliary sources.
14. J. Wassermann 1992 *DAGA* 92, 1001–1004. Sound radiation from a plate underwater using the equivalent source method.
15. A. D. Pierce 1989 *Acoustics*: *An Introduction to its Physical Principles and Applications*. Woodbury, New York: The Acoustical Society of America.
16. L. L. Beranek 1986 *Acoustics*. New York: American Institute of Physics.
17. P. M. Morse and K. U. Ingard 1986 *Theoretical Acoustics*. New York: McGraw-Hill.
18. M. L. Munjal 1987 *Acoustics of Ducts and Mufflers*. New York: John Wiley.
19. H. Fuchs and A. Michalke 1973 *Progress in Aerospace Sciences* **14**, 227–297. Introduction to aerodynamic noise theory.
20. A. Michalke 1972 *Zeitschrift der Flugwissenschaft* **20**, 229–237. An expansion scheme for the noise from circular jets.
21. B. J. Tester 1973 *Journal of Sound and Vibration* **28**, 151–203. The propagation and attenuation of sound in lined ducts containing uniform ''plug'' flow.
22. A. Michalke 1990 *Journal of Sound and Vibration* **142**, 311–341. On experimental sound power determination in a circular pipe with uniform mean flow.
23. A. Michalke 1971 *Ingenieur-Archiv* **40**, 29–39. Der Einfluß variabler Dichte auf die Instabilität einer freien Scherschicht.